**FULL PAPER**

# Observations of co-existing rising and falling tone emissions of electromagnetic ion cyclotron waves

Biswajit Ojha[1*] , Yoshiharu Omura[2], Satyavir Singh[3] and Gurbax S. Lakhina[4]

## Abstract

We report observations of co-existing rising and falling tone emissions of electromagnetic ion cyclotron (EMIC) waves by THEMIS E spacecraft. The investigation of these fine structures of the EMIC waves is essential from the point of view of understanding the connection between the proton holes and the proton hills in velocity phase-space. The wave packets of rising and falling tones are tracked by Poynting vector analysis, where we observe that the rising tones are propagating northward and the falling tones are propagating southward. The nonlinear wave growth theory supports our observations. We propose a model where the proton velocity distribution function evolves through the formation of proton holes on the negative side of the distribution function and mirrored resonant protons forming proton hills on the positive side of the distribution function, allowing us to observe the co-existing rising and falling tone EMIC waves.

**Keywords**  Fine structures of rising and falling tone EMIC waves, Nonlinear evolution of the velocity distribution function
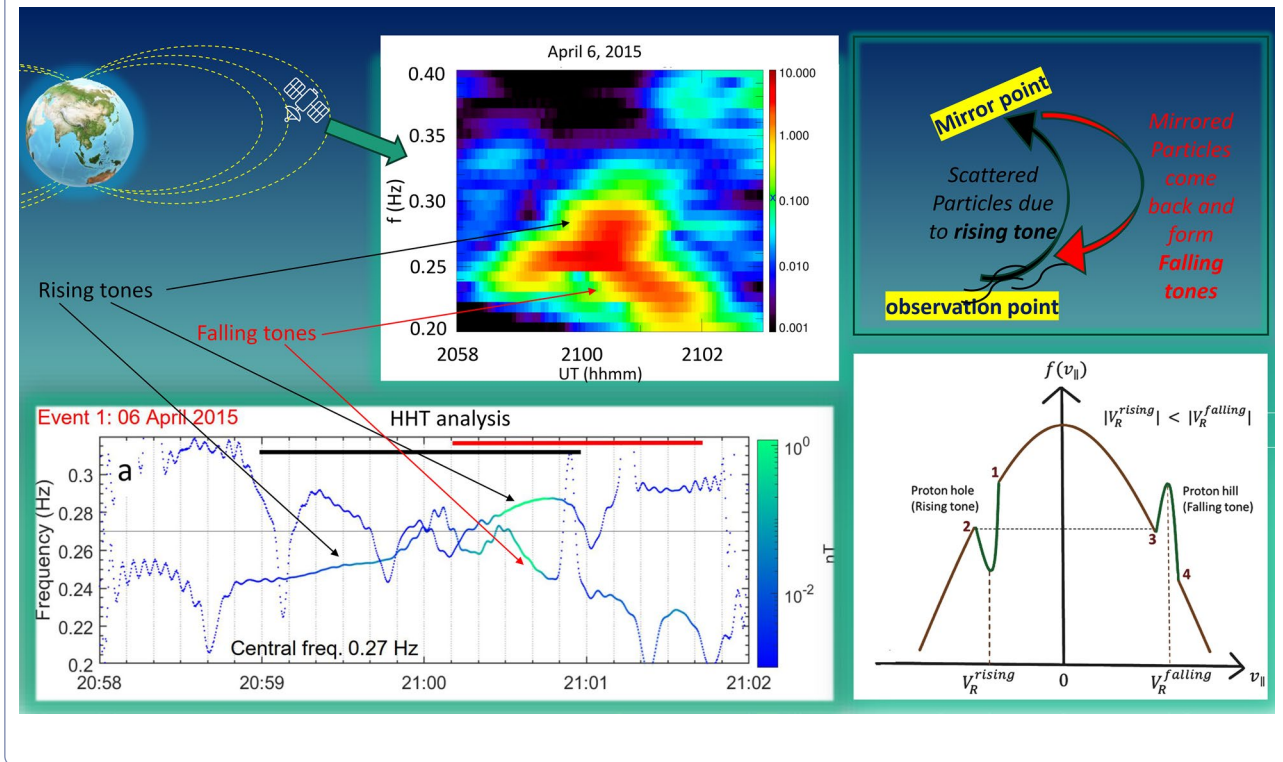
*Correspondence:
Biswajit Ojha
bojha92@gmail.com
Full list of author information is available at the end of the article

**Graphical abstract**



## Introduction

Electromagnetic Ion Cyclotron (EMIC) waves are observed below proton gyrofrequency and are generated with left-hand polarization generally around the geomagnetic equator (±11° MLAT) due to the hot proton temperature anisotropy ($T_\perp/T_\parallel > 1$) (Gendrin et al. 1984; Engebretson et al. 2008; Kivelson and Russell 1995; Clilverd et al. 2015; Allen et al. 2015). Recent studies (Vines et al. 2019) have also reported off-equatorial local generation because of minimum B-pockets (B is the magnetic field) produced by drift-shell splitting and Shabansky orbits (McCollough et al. 2010; Shabansky 1971). For larger L-shell, drift shell splitting would provide higher ion anisotropy due to plasma convection at dayside magnetosphere (Sibeck et al. 1987) and leads to the generation of these waves at off-equatorial latitudes. Assuming the presence of ion species (e.g., $H^+$, $He^+$, $O^+$, etc.), EMIC waves are divided into three bands, namely, H-band, He-band, and O-band (Saikin et al. 2015; Kozyra et al. 1984).

These waves often have fine structures consisting of many coherent subpackets (Grison et al. 2013; Nakamura et al. 2015; Pickett et al. 2010), which are generated nonlinearly after the linear growth due to the proton temperature anisotropy; the rising tones are generated through the formation of proton holes in velocity phase-space, whereas the falling tones are generated by proton hills (Shoji and Omura 2013; Omura et al. 2010; Nakamura et al. 2014; Shoji and Omura 2013; Omura and Zhao 2012). The nonlinear wave growth of these rising and falling tones has been reproduced in a self-consistent hybrid simulation by Shoji and Omura (2011). Recently, Ojha et al. (2021) have shown from THEMIS observations that the nonlinear growth of these subpackets is very rapid because these subpackets can change their amplitudes and frequencies within one wavelength, supporting the nonlinear theory and simulation. Nakamura et al. (2016) performed a statistical study of rising and falling tones from the THEMIS spacecraft observations and reported that the occurrence of rising tones is higher than the falling tones. Further, subpacket structures were found in 70% of EMIC rising or falling tones observed in the dayside magnetosphere. In contrast, the subpacket occurrence rate is much lower in constant tone EMIC waves. Their survey of THEMIS burst mode data from 2008 to 2011 has also reported the non-existence of apparent rising and falling tones below 5 $R_E$ from the Earth. These rising tones are also found in ground observations. Kakad et al. (2018) presented

Ojha *et al. Earth, Planets and Space*       (2024) 76:81

Page 3 of 19

a detailed analysis of the subpacket structures found in rising tones. Their statistical study has reported that more than 70% of rising tones are right-handed, indicating the polarization reversal of these L-mode waves due to crossover frequency while propagating to higher latitudes along the magnetic field (Horne and Thorne 1993).

The rising tones can strongly resonate with relativistic electrons and scatter them into a loss cone (Omura and Zhao 2012). Studies have also shown significant loss of relativistic electrons due to nonlinear resonant pitch angle scattering by EMIC waves (Omura and Zhao 2013; Usanova et al. 2014; Kubota et al. 2015; Ni et al. 2015; Zhang et al. 2016; Nakamura et al. 2019; Hendry et al. 2019; Zhu et al. 2020). Recently, Shoji et al. (2021), in a case study from ARASE spacecraft observation, has confirmed the existence of proton hill, which is considered as proton density enhancement in the velocity phase-space due to nonlinear trapping of protons by the wave field. They have discussed the wave–particle interaction analysis (WPIA) method (Katoh et al. 2013) to identify how nonlinear currents generate rising and falling tones, which are increasing and decreasing of frequencies of EMIC waves. Shoji et al. (2021) have also shown that there exists a complicated signature (see Fig. 2a of their paper) of increasing frequency (rising tone), and thereafter, the falling tones are observed quite prominently. Studies in the past have shown the distinct occurrence of rising and falling tone EMIC waves, and have not reported simultaneous observation of rising and falling tones (Grison et al. 2013, 2018; Pickett et al. 2010; Nakamura et al. 2014, 2015). We present detailed observations to explain these fine structures of EMIC waves where co-existing rising and falling tones are observed. Three events observed by THEMIS E spacecraft are investigated to explain these fine structures. The data sources and analysis methods and the detailed observations of each event are described in the data analysis and observation, Sect. 2. In Sects. 3 and 4, we have validated our observations with the nonlinear theory and postulated a model for these observations of co-existing rising and falling tones. Our findings are discussed and summarized in the Sect. 5.

## Observations and data analysis

We use the Time History of Events and Macroscale Interactions during Substorms (THEMIS) spacecraft's electric field instrument (EFI) data (8 Hz sampling rate) for electric field (Bonnell et al. 2009) and fluxgate magnetic field (FGM) data (4 Hz sampling rate) for magnetic field (Auster et al. 2008). These data are then transformed into field-aligned coordinates (FAC), where the x-axis is the Earth–sun line, the z-axis is along the Earth's magnetic field, and the y-axis completes

the orthogonality. The magnetic field data are then bandpass filtered (we used the Butterworth filter with the Hanning window) for the desired frequencies, and the wave magnetic fields are calculated. Further, from the data, the parallel component of the electric field is calculated by the assumption **E.B**=0. We down-sampled the electric field data from 8 to 4 Hz for the Poynting flux calculation to match with the FGM data. The high-frequency resolution (HFR) plots are obtained by using a window size of 128 s (512 samples) with shifting the fast Fourier transform (FFT) window by 4 s (Ojha et al. 2021). We use SPEDAS tool for calculating the wave parameters (Angelopoulos et al. 2019). The detailed analysis of the observations of three co-existing falling and rising EMIC tone events are presented in the next section.

To see the corresponding particle properties, we have calculated the ion velocity distribution functions from the electrostatic analyzer (ESA) and solid-state telescope (SST) data, where ion energy flux is measured for energy ranges 5 eV–25 keV and 25 keV–6 MeV, respectively (McFadden et al. 2008). The pitch angle distributions (PADs ) are plotted in the FAC coordinates over a full gyrophase of protons and within a specified energy range for each event.

### Event 1: 6 April 2015

We present the first event observed on 6 April 2015 by THEMIS E spacecraft at dayside outer magnetosphere. The magnetopause position is calculated by the magnetopause model described in Shue et al. (1998), and it shows the spacecraft was very close but inside $\sim 0.4\ R_E$ from the magnetopause boundary with a radial distance $\sim 10.5\ R_E$ from the Earth. In Fig. 1, the wave properties are shown from 20:54 UT to 21:06 UT, whereas the event occurred from 20:58 UT to 21:02 UT. The magnetic latitude (MLAT) and magnetic local time (MLT) calculated from TS04 model Tsyganenko (2005) are MLAT $\sim 15.4°$ north and MLT $\sim 13.1$ h. We have checked the solar wind conditions (not shown here), where no significant change in solar wind dynamic pressure is perceived. However, a rotation in IMF Bz is observed just before the event. Thus, dayside reconnection and the injection of thermal particles are expected (Zhang et al. (2022) and references therein).

In Fig. 1a, the total perpendicular magnetic field spectra are shown. The magenta dashed curve denotes the local helium gyrofrequency ($f_{cHe^+}$). We first look into the wave power spectrum to recognize the co-existing rising and falling frequencies. From closer visual inspection, we identify this event in the proton band, showing a rising tone from 20:59 UT, and a simultaneous rising and a falling tone after 21:00 UT. The rising tone contains frequencies from 0.27 Hz to 0.32 Hz, whereas
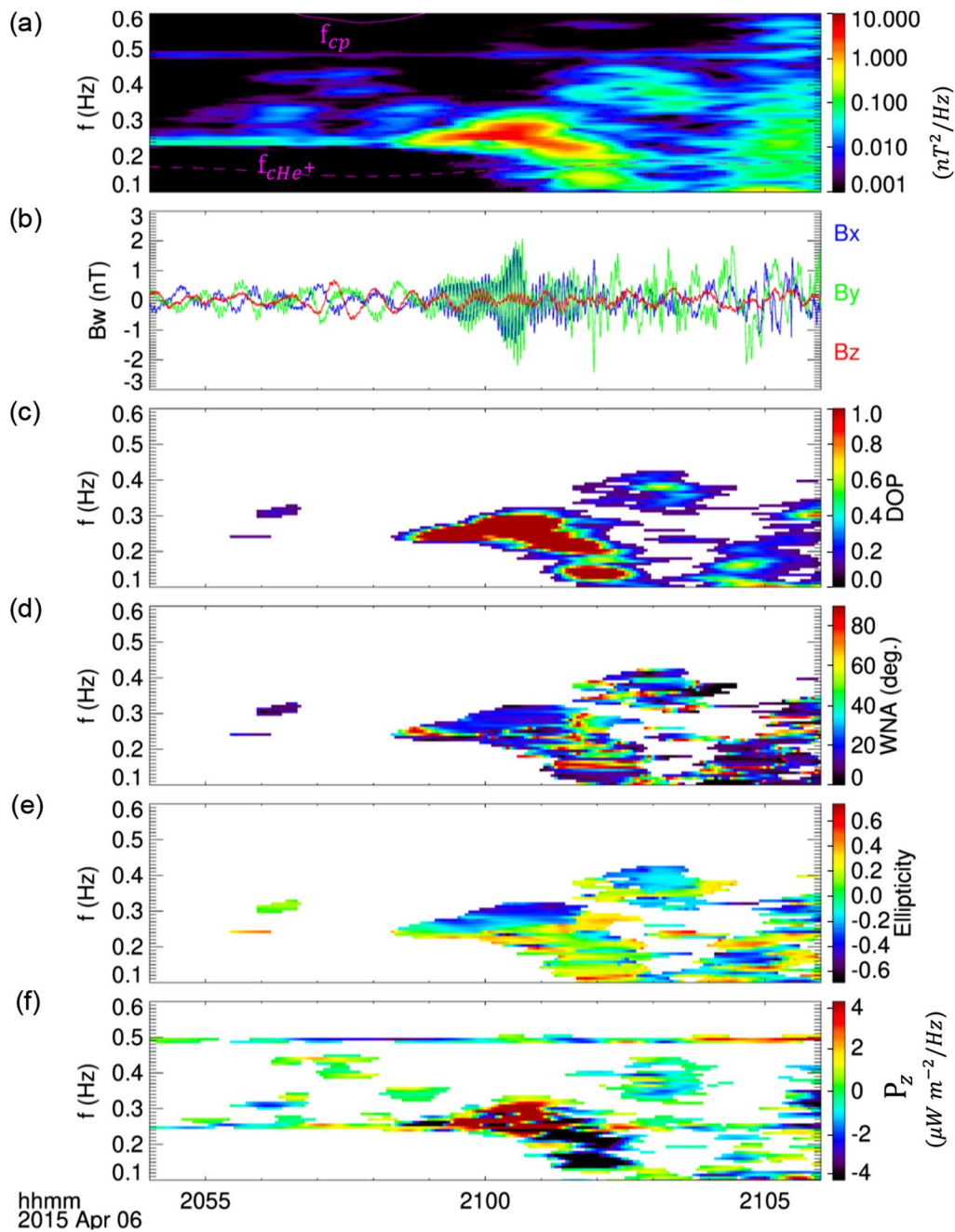
**Fig. 1** Event 1: 6 April 2015, wave properties: **a** Power spectrum of the total perpendicular magnetic field, $B_\perp$ with colorbar show power spectral density in $nT^2/Hz$, magenta dashed line shows the helium gyrofrequency ($f_{cHe+}$) and the solid blue line is proton gyrofrequency ($f_{cp}$), **b** magnetic field components of the waves in field aligned coordinates (FACs) ($B_x$, $B_y$, and $B_z$ in blue, green, and red, respectively), **c** degree of polarization, **d** wave normal angle, **e** wave ellipticity; negative for left-handed (LH) and positive for right-handed (RH), **f** parallel component of the Poynting vector ($P_Z$)

the falling tone contains 0.27–0.20 Hz. A detailed analysis of these simultaneous rising and falling tones is provided later in the paper, Fig. 1b shows the FAC components of magnetic fields (**B**) where the $\mathbf{B}_\parallel$ ($\mathbf{B}_Z$) is in red and the other perpendicular components $\mathbf{B}_\perp$ ($\mathbf{B}_X$ and $\mathbf{B}_Y$) are in blue and green, respectively. We see the dominant $\mathbf{B}_\perp$ in this plot, which is typical for EMIC waves. The observed wave amplitudes are ~1–2% of the total background magnetic field (~45.8 nT).

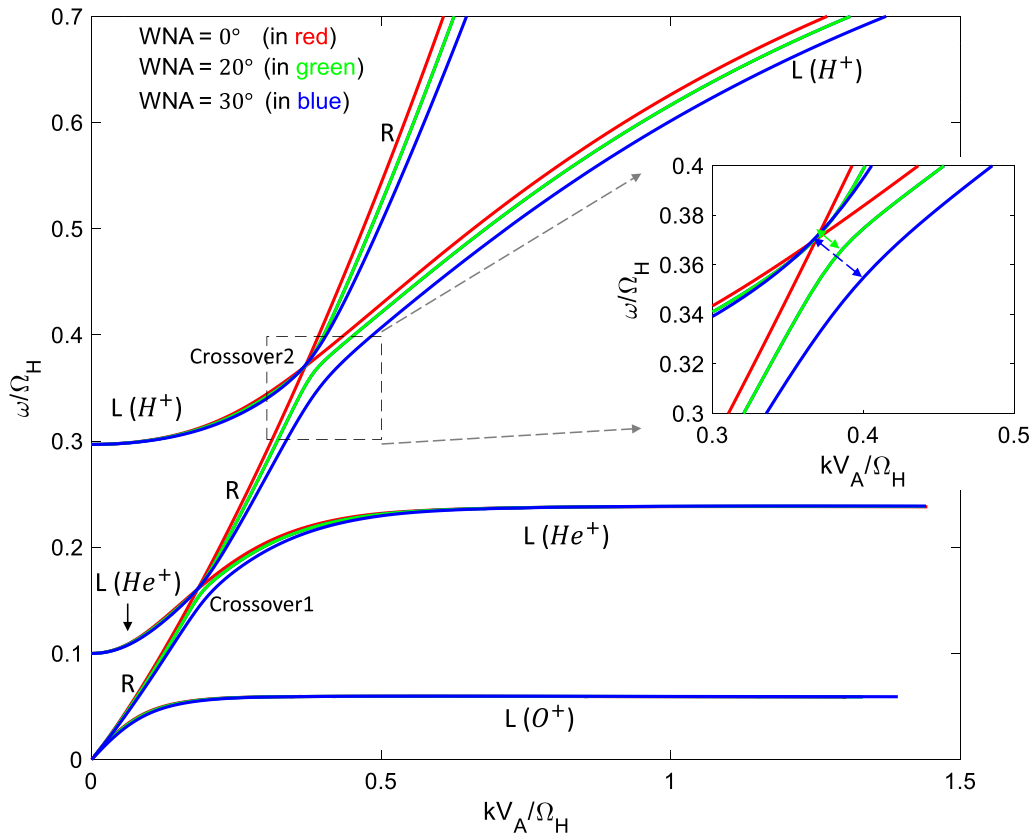**Fig. 2** Linear dispersion relation of EMIC waves for a plasma comprising of $H^+$, $He^+$, $O^+$, and $e^-$ for $0°$, $20°$, and $30°$ in red, green, and blue, respectively. '$R$' denoting right-handed mode while '$L$' is left-handed mode. Crossover can be seen for the finite angles of propagation. In the inset zoomed portion is shown, where the gap between the dispersion surfaces can be seen for finite angles

In Fig. 1c, the wave degree of polarization (DOP) shows high values (close to 1), suggesting the observed waves have high planarity, hence, the plane wave approximation for the wave properties analysis is valid. There are empty spaces in Fig. 1c–e as wave amplitude threshold of 0.1 nT was applied. We plot only those frequencies where the wave amplitude is greater than 0.1 nT. However, for Fig. 1f, we only plot those values where Poynting flux values are greater than 1.0 $\mu Wm^{-2}Hz^{-1}$. The wave normal angles (WNAs) are shown in Fig. 1d. The rising and falling tones propagate nearly parallel ($\leq 30°$) to the ambient magnetic field. These waves with frequency $\sim$ 0.15 Hz lies on or just below $f_{cHe^+}$ and are quite oblique (WNA$> 70°$). In the wave ellipticity spectrum in Fig. 1e the values are calculated from -1 to +1, but shown only $-0.6$ to $+0.6$ for better visual. Figure 1e shows the rising tones with left-handed polarization as they have negative ellipticity. In contrast, linear and right-handed polarization is observed for the falling tones. We consider this polarization change due to the crossover frequency where the left-hand mode turns into the right-hand mode. We have explored this possibility by plotting the

dispersion relation in Fig. 2. Considering heavy ions ($He^+$ and $O^+$) in the plasma system, we plot dispersion curves, $\omega/\Omega_H$ as a function of $kV_A/\Omega_H$, where $\omega$ is wave frequency, $\Omega_H$ is the proton gyrofrequency, $V_A = B/\sqrt{\mu_0\rho}$ is the Alfven velocity, B is the total magnetic field, $\mu_0$ is the permeability of the vacuum, and $\rho$ is the total mass density of charged plasma particles. For proton, helium, and oxygen bands, the dispersion curves show for the wave normal angles $0°$, $20°$, and $30°$ in red, green, and blue, respectively. There are two crossovers: crossover 1 between $He^+$ band and R-mode, and crossover 2 between $H^+$ mode and R-mode. In the inset, the zoomed portion shows the gap between two green lines (for $20°$, separation indicated by a dashed green double arrow) and between two blue lines (for $30°$, separation indicated by a dashed blue double arrow), but two red lines (for $0°$) cross each other. The scenario is the same for the crossover 2. This is because the crossover occurs between R- and L-modes at finite propagation angles, and we expect linear polarization at the crossover frequency.

Figure 1f shows the parallel component of the Poynting vector ($P_z$). The colorbar shown here is spectral density

Ojha *et al. Earth, Planets and Space*     (2024) 76:81

Page 6 of 19

Event 1: 06 April 2015

Event 2: 13 April 2015
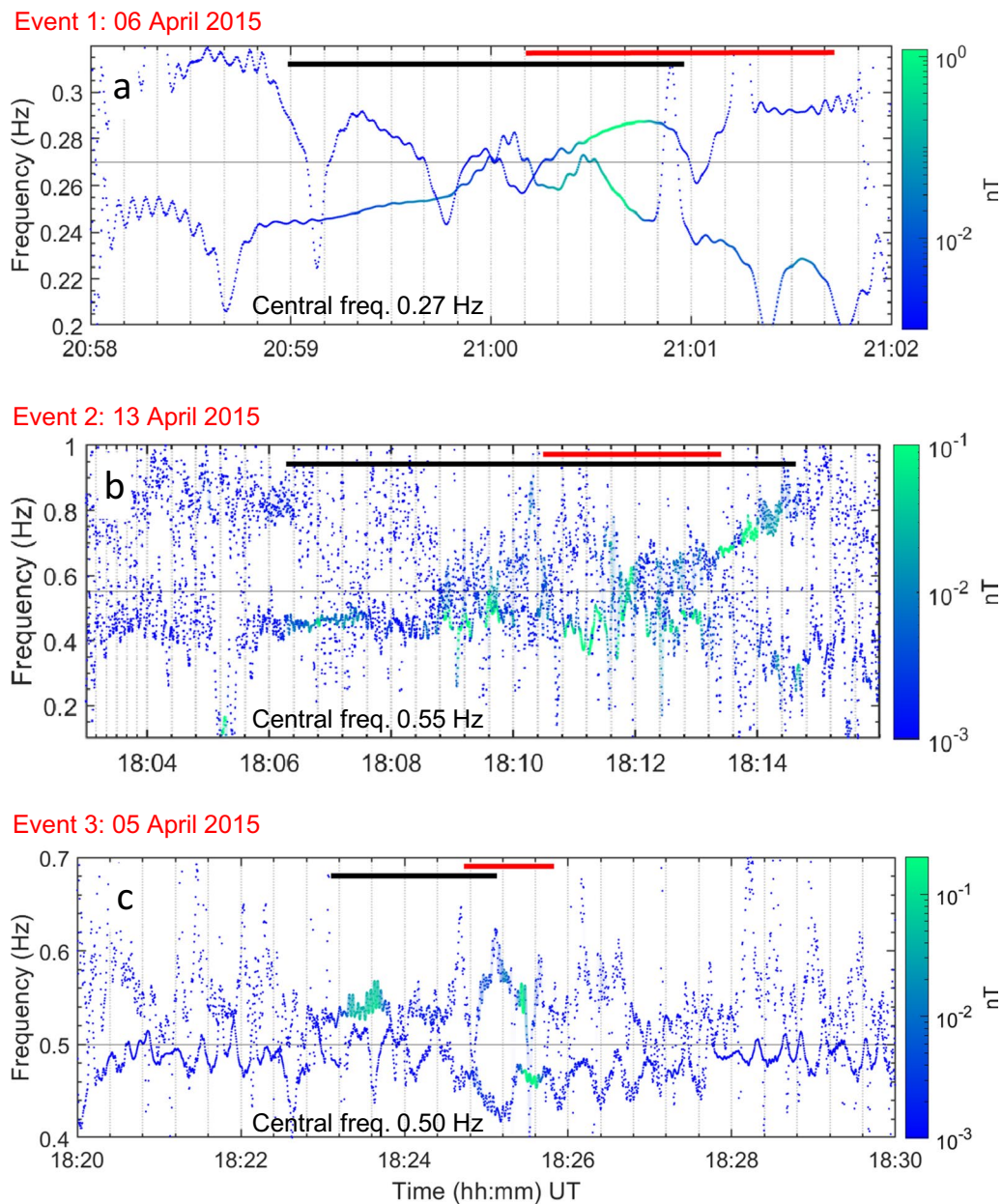
Event 3: 05 April 2015

**Fig. 3** Instantaneous frequencies and amplitudes calculated from the HHT method for both falling and rising tones. The color bar shows the instantaneous amplitudes. The horizontal bold red line denotes falling tone timing, while the bold black line denotes timing for rising tone. The black line at the center of each panel denotes the central cut to use the bandpass filter for the rising and falling tones. **a** Event 1: falling (0.27–0.20 Hz) and rising (0.27–0.32 Hz) from 20:58 to 21:02 UT, **b**: falling ( 0.55–0.10 Hz) and rising ( 0.55–1.0 Hz), **c** Event 3: falling ( 0.5–0.4 Hz) and rising ( 0.5–0.7 Hz)

in $\mu Wm^{-2}Hz^{-1}$. Here, positive (negative) $P_z$ means the waves propagate northward (southward). We see both red and blue patches showing bidirectional flows of wave energy. A closer inspection reveals that the rising tone is predominantly northward, while the falling tone propagates southward. The vital point is a parallel and antiparallel flow of ion populations is expected for the

cyclotron interaction with the bi-directional EMIC rising and falling tones.

### Instantaneous frequency and amplitude variation

To strengthen our interpretation of rising and falling tones together, we analyze instantaneous frequencies. In Fig. 3, we calculate the instantaneous frequencies and

instantaneous amplitudes by Hilbert Huang Transformation (HHT) method (Huang et al. 1998; Huang 2014; Shoji et al. 2018; Ojha et al. 2021). This method has high accuracy in dealing with nonlinear waves. Initially, a signal is decomposed into several intrinsic mode functions (IMFs) by an empirical mode decomposition (EMD) method. Thereafter, Hilbert transform applies to the IMFs, and we get instantaneous frequencies and amplitudes. Although, this method has a high accuracy to deal with nonlinear and nonstationary signals, there can be mode mixing when empirical mode decomposition is done. We have investigated the intrinsic mode functions after decomposing the original signal, and confirmed no mixing is there for all the events. From the visual inspection in Fig. 3a, we see a larger wave power for the rising and falling frequencies from 0.27 Hz.

Primarily, through visual inspection, we apply an ideal bandpass Butterworth filter for the lower band (containing falling frequencies) is from 0.27 Hz to 0.20 Hz, and the upper band (containing rising frequencies) is from 0.27 Hz to 0.32 Hz. We have checked the desired band pass filter efficiency by adopting the transfer functions and zero-pole-gain methods (Jackson 1989; Mitra 2006). In both cases, the filter works well and produces similar results which confirm that there is no artifact in the rising and falling frequency bands.

Figure 3 shows the instantaneous frequency derived from the most prominent intrinsic mode function (IMF) from the rising and falling wave bands. Instantaneous frequency analysis by HHT method also provides better estimation of the timings of these kind of nonlinear emissions. We plot the instantaneous frequency as a function of time from 20:58 UT to 21:02 UT (for event 1) separately for the rising and falling bands and overplotted in a single figure. One may interpret the falling and rising frequency bands cross each other; however, it is not the case. The frequency variation in the rising band above the central frequency line is independent of the falling band and vice versa. Those variations for the two bands are overplotted in a single figure. The color bar shows the instantaneous amplitudes overplotted with each frequency component. In the figure, each dot denotes the frequency variation as well as the amplitude as a function of time. The dots are connected through a line which itself is colored according to the respective wave amplitude of the dots. The greener the dots are, the more amplitude they have, and they are considered true representation of the frequency variation. The remaining dots in blue, even though they are closely spaced for some frequencies, should not be considered as the true frequency variation as they have the lowest amplitudes. We calculated the frequency variation using spline interpolation in HHT, and therefore we see a lot of spikes.

The red and black horizontal lines in the figure denote the duration of the falling and rising tones, respectively. Thus, wherever the red and black line timing overlapped, we call it as simultaneous or in other words co-existing rising and falling tones.

For event 1, a rising tone patch with enough wave power (>0.1 nT, as we can also see from Fig. 1b) started earlier from 20:59 UT, as seen below the central line. Thus, we observe rising tones are present before the falling tones start. From ∼ 21:00:10 UT, simultaneous rising and falling frequencies are observed. The black and red lines show the timing of the observed rising and falling tones, and we estimate the duration of simultaneous observation ∼ 50 s. The rest of the blue dots are irrelevant as they have lower amplitudes than 0.1 nT, and they have spikes. This analysis confirms the frequency separation for this event.

**Event 2: 13 April 2015**
Event 2 was observed by THEMIS E on 13 April 2015 from 18:03 UT to 18:16 UT in dayside outer magnetosphere with MLAT ∼17.35° north, MLT ∼12.15 h and ∼8.75 $R_E$ away from the Earth. This time the solar wind dynamic pressure did not increase (not shown here); instead stayed ∼4 nPa throughout the event. The dynamic pressure remained high from ∼12 h before the event occurred. The measured AE index stayed at ∼ 100 nT from 1 h before the event. IMF Bz showed slight rotation (− 1 nT to 1 nT) at 18:00 UT, indicating a dayside reconnection.

Figure 4 shows the same panels as shown in Fig. 1. Figure 4a shows the perpendicular magnetic power spectrum for the bandpass filtered frequencies 0.1−1.0 Hz. The magenta dashed line denotes the local helium gyrofrequency ($f_{cHe^+}$). This structure is more complex than the first event. The rising tone starts from 18:06 UT and continues with low wave power until 18:11 UT. Thereafter, at 18:11 UT, we see strong power in the rising tone, and simultaneously, the falling tone starts. The patch below ∼0.2 Hz between 18:11–18:12 UT falls under the helium band. We identify the rising tone above 0.55 Hz and the falling tone below 0.55 Hz. In this case, in Fig. 4b, the FAC magnetic field components fluctuate, and the perpendicular components have higher magnitudes than the parallel ones. The DOP in Fig. 4c shows a high value thus have high planarity, hence, the plane wave approximation for the wave properties analysis is valid. The WNA (Fig. 4d) for this case shows a highly oblique propagation (∼80°) at 18:06 UT, and after that, the WNA decreased significantly, i.e., below 20°. For the rising tone starting at 18:11 UT, the WNA again shows nearly parallel propagation for both the rising and falling tones. Wave ellipticity in Fig. 4e for both rising and falling tones shows
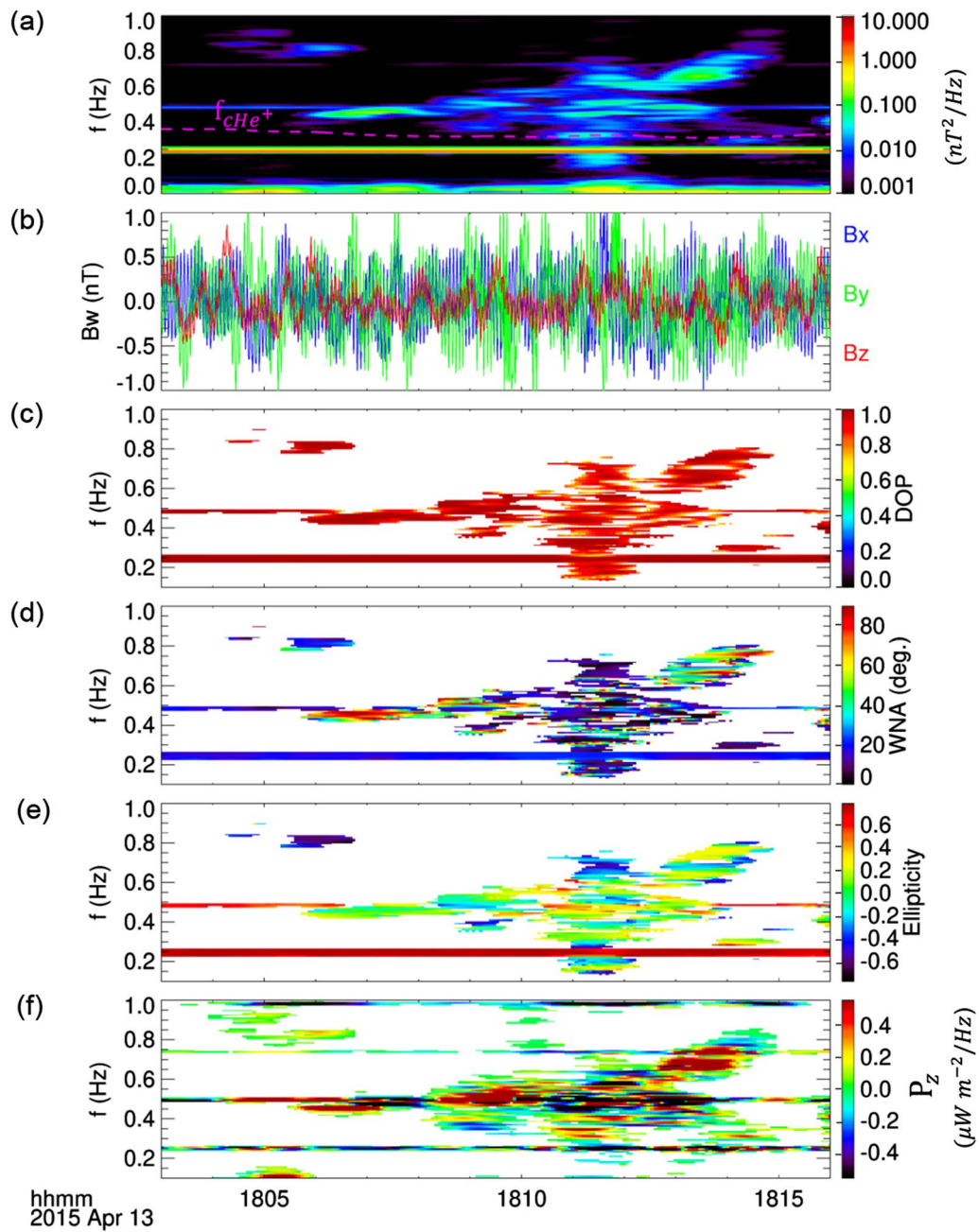
Ojha *et al. Earth, Planets and Space* (2024) 76:81

Page 8 of 19



**Fig. 4** Event 2: Panels are the same as in Fig. 1

the mixture of linear, left, and right-handed modes. We observe left-handed polarization for the rising tone patch at 18:11–18:12 UT above 0.6 Hz. We see linear and right-handed polarization for the rising tone emissions after 18:12 UT and almost linear polarization for the falling band, though the falling tone patch shows nearly parallel propagation. Even though the WNA is small, there is a chance of polarity reversal at the crossover frequency,

which makes the ellipticity linear and right-handed, as discussed in Event 1.

In Fig. 4f, both forward and backward waves are present as we observe both positive and negative $P_z$. We observe forward rising tone waves (red patches) before 18:10 UT and after 18:12 UT. The falling tone shows mostly backward wave propagation (black patches), except after 18:13 UT. During 18:10–18:12 UT, there was a mixture of both forward and backward propagation.

Ojha *et al. Earth, Planets and Space*    (2024) 76:81

Page 9 of 19

The instantaneous frequency analysis for this event is shown in Fig. 3b. Same as Event 1, we apply a bandpass filter from 0.55−1.0 Hz, and from 0.55−0.10 Hz containing rising and falling frequencies, respectively. The wave frequency rises, and high amplitude is observed around frequency ∼0.45 Hz starting from 18:06 UT lasted for 96 s (18:06:00 to 18:07:36 UT). Simultaneous rising and falling of wave frequencies are observed after 18:12 UT. The structure is very complex prior to 18:12 UT. We see traces of falling tones for ∼24 s (from 18:10:48 to 18:11:12 UT) and then rising tones from 18:11:12 UT. Thereafter, rising tones from 18:13:12 to 18:14:24 UT have amplified. The black line shows the existence of the rising tone before the first falling tone. As mentioned earlier, the dots represent data points, but scattered dots have no physical meaning unless those are close enough with high amplitudes as indicated by the green parts of the figure.

### Event 3: 5 April 2015

This event was observed on 5 April 2015 by THEMIS E at ∼8.4 $R_E$ from the Earth at ∼12.5 h MLT and 17.1 MLAT from 18:20–18:30 UT. During this event, no rotation in IMF Bz is observed. Figure 5a shows the total magnetic field power spectra 0.3−0.7 Hz. This event is also in the proton band ($f_{cp} \sim 1.3$Hz). The magenta dashed line denotes $f_{cHe^+}$. We observe waves with strong power ∼ 18:23−18:24 UT at 0.55 Hz. We observe frequency rising and falling simultaneously just before 18:25 UT. This structure, again, is a complex wave emission where one can see a lack of wave power between the $1^{st}$ patch and the later rising and falling patch (i.e., between 18:24–18:24:30 UT at ∼0.5 Hz). We have divided the upper band from 0.5−0.7 Hz and the lower band from 0.4−0.5 Hz. In Fig. 5b, a considerable enhancement in the magnitude of one of the perpendicular magnetic field components $B_y$ (in green) is observed as compared to the other two wave magnetic field components. The perpendicular wave amplitudes are 0.6−1.0% of the total background field (∼86 nT). The waves are highly coherent as DOP for this event also shows a high value close to 1 in Fig. 5c. In Fig. 5d, WNA broadly shows almost parallel wave propagation except for the frequency ∼0.5 Hz. The ellipticity in Fig. 5e shows a mixture of left and right-handed waves but mostly linear polarization. Poynting vector in Fig. 5f shows the parallel and antiparallel wave propagation. In this case, the 1st patch and falling band propagate parallel, whereas the rising tone is antiparallel. At some frequencies, the WNA is large for all three events, but the $P_z$ is still parallel or antiparallel. This is due to the propagation effect of these wave packets. The observed waves traveled away from the source region, making the oblique propagation, but primarily the wave energy traversed

along the parallel or antiparallel to the background magnetic field.

In this event, the instantaneous frequency analysis showed a band from 0.5−0.7 Hz containing rising frequencies, and another band from 0.5−0.4 Hz containing falling frequencies in Fig. 3c. This figure shows that the first patch at ∼18:23–18:24 UT has a frequency spread towards higher values, i.e., it is a rising tone emission. Moreover, from 18:24:48 UT, simultaneous rising and falling frequencies are seen for a short time (∼ 24 s), and thereafter, decrease in frequency is seen from 18:24:48 UT to 18:25:12 UT. The best estimation gives a frequency decrease from 0.62 Hz to 0.5 Hz. This falling tone is prominent, and it has a higher wave amplitude. Like the other two events, the rising tone exists prior to the falling tone, as indicated by the black and red lines.

## Theoretical model analysis for the observed wave
### Theoretical velocities

We compare our observational results with theoretical understandings in this section for all three events. Assuming the cold plasma dispersion relation [Stix (1962)] for multi-species plasmas, the phase velocity ($V_p = \omega/k$, where $\omega$ is the wave frequency and k is the wavenumber), the group velocity ($V_g$) calculated from the Eq.(22) of Omura and Zhao (2012) assuming the parallel propagation (as WNA is mainly parallel to the ambient magnetic field for all the events) and the resonance velocity ($V_R$) calculated from the cyclotron resonance condition are plotted in Fig. 6.

The plasma is comprised of three ion populations ($H^+, He^+$, and $O^+$) and electrons, $e^-$. For event 1, the observed total plasma density ($n_e$) is 5 $cm^{-3}$, and the ion composition ratios are ($n_p : n_{He^+} : n_{O^+}$) = (0.90: 0.05: 0.05). The hot protons are 1% of the total proton population (see Table 1). For these parameters, we have first checked that the observed wave amplitudes for these events are well within the nonlinear threshold and optimum amplitudes as discussed by Ojha et al. (2021) and Shoji and Omura (2013). We plot the theoretical velocities for three bands ($H^+, He^+$, and $O^+$) with the varying frequencies in Fig. 6. For each event the dashed-dot represents the lowest frequency of the falling tones, and the solid line represents highest frequency of the rising tone; whereas the dashed line denotes the starting frequency for the rising tone. Careful observation shows that for event 1 they are 0.23 Hz, 0.27 Hz, and 0.32 Hz, for event 2 those are 0.4 Hz, 0.55 Hz, and 0.8 Hz, and for event 3 those are 0.4 Hz, 0.5 Hz, and 0.7 Hz. Since the waves interact with the counter-streaming protons, we plot negative $V_R$. In the proton band, $|V_R| > V_g$ is the necessary condition for the nonlinear interaction between the wave and the protons (Nogi and Omura 2021). The condition
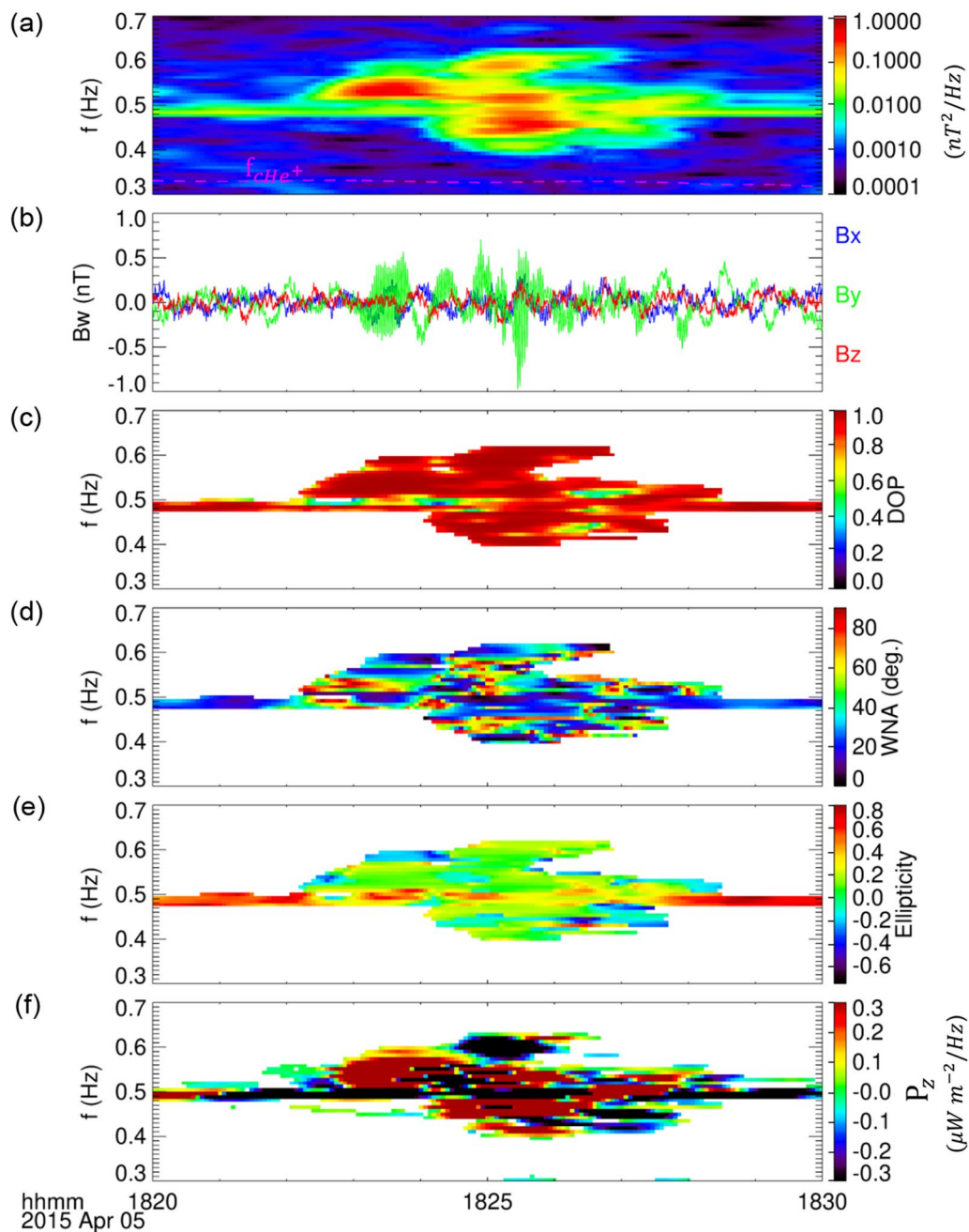
Ojha *et al. Earth, Planets and Space*      (2024) 76:81

Page 10 of 19



**Fig. 5** Event 3: Descriptions are the same as the other two events

$-V_R > V_g$ is necessary for a new emission to be generated upstream from the triggering wave. The wave packet generated upstream undergoes effective nonlinear wave growth through propagation in the generation region. The theoretical values of $-V_R$, which is $\sim 400 - 2000$ km.s$^{-1}$ for the event 1 (and valid for all the events), match very well with the observed proton parallel velocities $\sim 500-1500$ km.s$^{-1}$ (from the proton velocity distribution cut across the perpendicular direction to the backround field; not shown here). This indicates the possibility of nonlinear cyclotron wave–particle interaction. We also observe that $V_P >> V_g$ for this event, which suggests the Landau resonance cannot occur (Ojha et al. 2021).
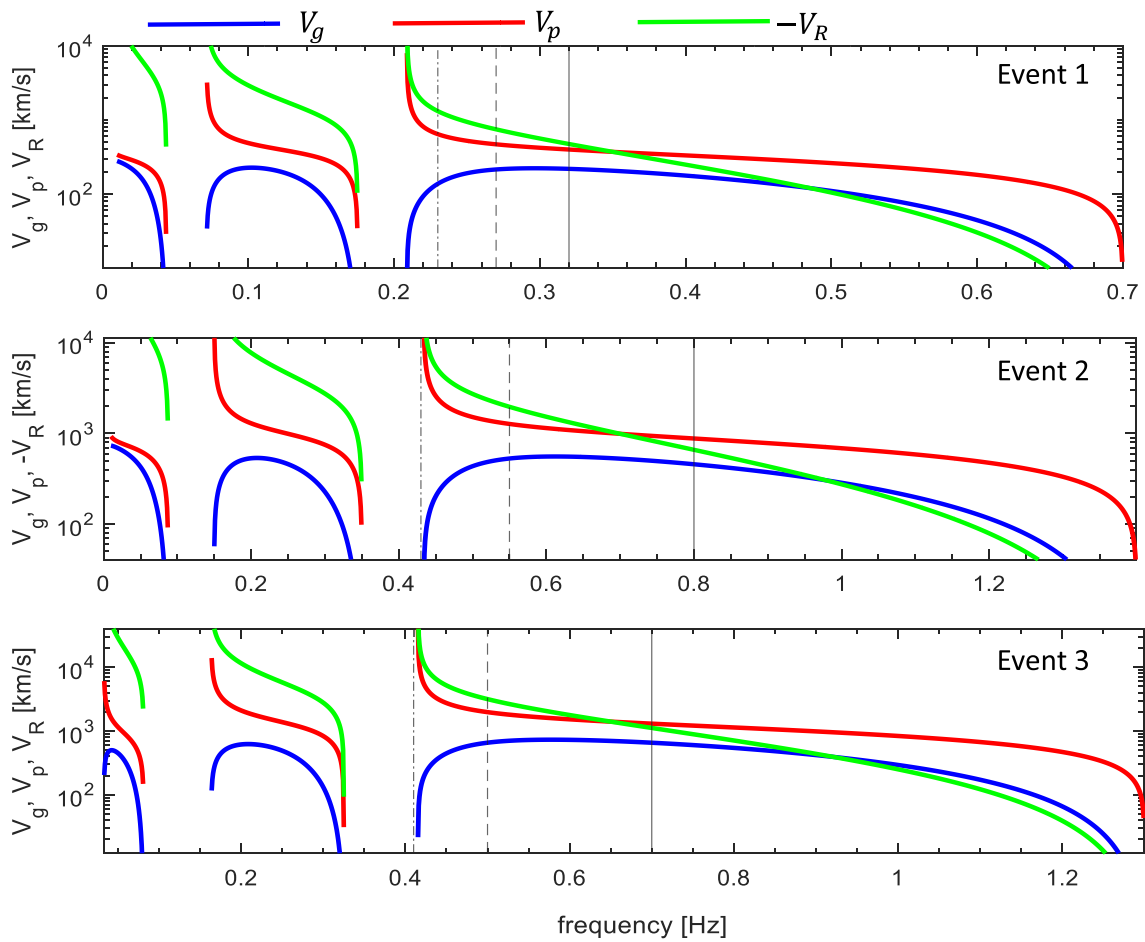
Ojha *et al. Earth, Planets and Space* (2024) 76:81

Page 11 of 19



**Fig. 6** Theoretical velocities $V_g$, $V_p$, and $-V_R$ (group, phase, and resonance velocity in blue, red, and green, respectively) are plotted as function of frequencies for $H^+$, $He^+$, and $O^+$ bands. For each event the dashed-dot, dashed, and solid lines represent the lowest frequency of the falling tone, starting frequency for the rising tone, and highest frequency of the rising tone emission

**Table 1** For theoretical calculations, the total plasma density values are estimated from the ESA probe data and the composition ratios are calculated following Omura et al. (2010)

| Parameters | Event 1 | Event 2 | Event 3 |
|---|---|---|---|
| $n_e$ (cc) | 5.0 | 3.0 | 1.5 |
| cold $n_p/n_e$ | 0.8900 | 0.8712 | 0.8811 |
| hot $n_{ph}/n_e$ | 0.0100 | 0.0088 | 0.0089 |
| cold $n_{He+}/n_e$ | 0.050 | 0.060 | 0.055 |
| cold $n_{O+}/n_e$ | 0.050 | 0.060 | 0.055 |
| $B_{mag}$ (nT) | 45.80 | 91.00 | 85.15 |

## Evolution of proton velocity distribution

Based on our observations we propose a model that can generate both rising and falling tones. The generation of co-existing rising and falling tones could be due to the evolution of the proton velocity distribution in phase space. All three events show that there exist wave packets with enhanced wave amplitude (nT) or spectral density (nT$^2$/Hz) before the simultaneous rising and falling tones are observed. This is seen for Event 1 from 20:59–21:00 UT (Fig. 1), for Event 2 from 18:06–18:10 UT (Fig. 4), and for Event 3 from 18:22–18:24 UT (Fig. 5). These patches are observed as rising tones for all three events and can scatter the resonant protons into smaller pitch angles, making larger parallel velocities. The scattered protons can bounce from the other hemisphere and return to the same point where they interacted with the wave packet but in the opposite direction.

## Theoretical minimum resonance energy for the observed EMIC waves

In Table 1, we have listed the parameters which are used to calculate the resonance energy; $n_e$, hot $n_{ph}$, cold $n_p$, cold $n_{He+}$, cold $n_{O+}$ are densities of electrons, hot protons,
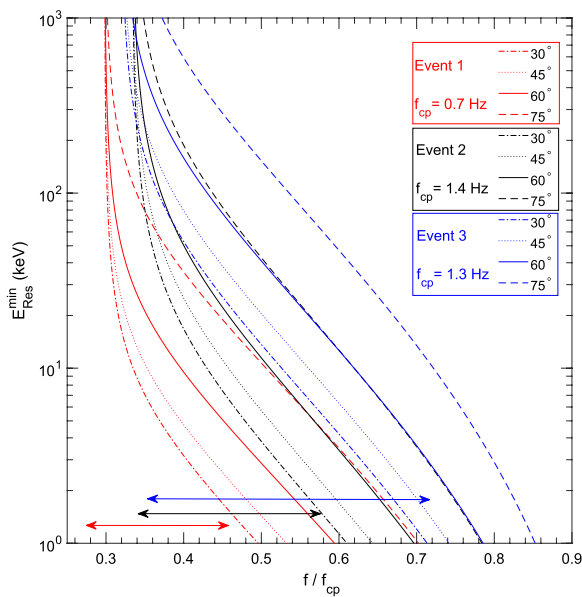
**Fig. 7** Minimum cyclotron resonance energy $E_{Res}^{min}$ as a function of normalized frequency ($f/f_{cp}$) for pitch angles 30° (dashed-dot), 45° (dotted), 60° (solid), and 75° (dashed) curves in red for Event 1 ($f_{cp} =$ 0.7 Hz), black for Event 2 ($f_{cp} = 1.4$ Hz), and blue for Event 3 ($f_{cp} = 1.3$ Hz). The observed frequency range is indicated by the double-arrows in red, black, and blue colors for Events 1, 2, and 3, respectively

cold protons, cold heliums, cold oxygens, and $B_{mag}$ is the total background magnetic field. The total plasma density and the ion densities are estimated from the ESA probe data and the heavy ion compositional ratios are calculated following the Omura et al. (2010), where by calculating the cutoff frequencies, and using the dispersion and charge neutrality condition we can estimate the compositional ratios. We first calculated the theoretical resonance energies assuming parallel wave propagation and the first order resonance condition for all three events to get the cyclotron energy range. Figure 7 shows the theoretical minimum resonance energies ($E_{Res}^{min}$) vs normalized frequencies ($f/f_{cp}$) for the observed three events ($f_{cp}$ being the corresponding proton cyclotron frequency). We calculated $E_{Res}^{min}$ for the different pitch angles 30° (dashed-dot), 45° (dotted), 60° (solid), and 75° (dashed) curves with red for Event 1 ($f_{cp} = 0.7$ Hz), black for Event 2 ($f_{cp} = 1.4$ Hz), and blue for Event 3 ($f_{cp} = 1.3$ Hz). We denote the observed frequency ranges with the double arrows in red, black, and blue colors for Events 1, 2, and 3, respectively. At a particular frequency, the $E_{Res}^{min}$ increases with increasing pitch angles, which should be consistent for all three events. For Event 1 the $E_{Res}^{min}$ spans in a range ~2–20 keV for different pitch angles, for Event 2 it spans in ~2–30 keV, and for Event 3 the energy spans in ~2–100 keV. We neglect the asymptotic portions of the curves towards the lower frequencies to avoid incorrect energy values.

It should be noted that there is a stop band for L-mode propagation between $He^+$ and $H^+$ band. However, we observe wave signatures in those frequencies. According to the wave ellipticity observed for all three events, we see linear and right-handed polarization, which can be seen as the crossover occurred. We also note that because of the scattered source regions of EMIC waves (Ojha et al. 2021) near the geomagnetic equator, the sub-packets can be observed in the source regions with different ellipticity. This illustration is important for choosing the correct energy range for the cyclotron interaction with the protons and comparing it with the observational proton pitch angle distributions (PADs).

**Proton pitch angle distributions (PADs)**

To see the energetic particle properties, we have calculated the ion velocity distribution functions from the ESA probe and SST probe data, where ion energy flux is measured for energy ranges 5 eV–25 keV and 25 keV–6 MeV, respectively (McFadden et al. 2008). Figure 8 shows the pitch angle distributions (PADs) for all three events in the FAC coordinates over a full gyrophase of protons for a range of energies that matches with the theoretical resonance energies shown in Fig. 7. The colorbars in 8 shows observed proton flux in $eV/(s.cm^2.str.eV)$. The first panels for each event in Fig. 8 shows the dynamic power spectra for the reference. From the theoretical resonance energy ($E_{Res}^{min}$) calculation, we know which range of the energies we should look at for the PADs. Our goal is to discuss the following three phenomena

- scattering of the protons by EMIC rising tone waves,
- bounce motion of the protons, and
- trapping of the protons by nonlinear potential to form proton hill and falling tone waves.

For clarity, we plot PADs for Event 1 and Event 2 from the ESA probe data for the energy channels 6.9 keV, 9.1 keV, 11.9 keV, 15.7 keV, and 20.7 keV. For Event 3, the energy channels plotted are 15.7 keV, 20.7 keV, 25–40 keV, 40–60 keV, and 60–100 keV. We can think of the vertical axis in two directions, one for the parallel direction (below 90°) and the other for antiparallel direction (above 90°). In each energy panel, each pixel represents energy flux corresponding to respective time at a particular pitch angle. When a group of particles is scattered by the EMIC wave, the density of the particles close to 90° pitch angle (which are responsible for the anisotropic energy distribution, hence the free energy source for the wave growth) will reduce, and we observe higher particle density in the lower pitch angles.

Figure 8 shows the most prominent feature in the energy channel 11.9 keV for Event 1 and Event 2, where
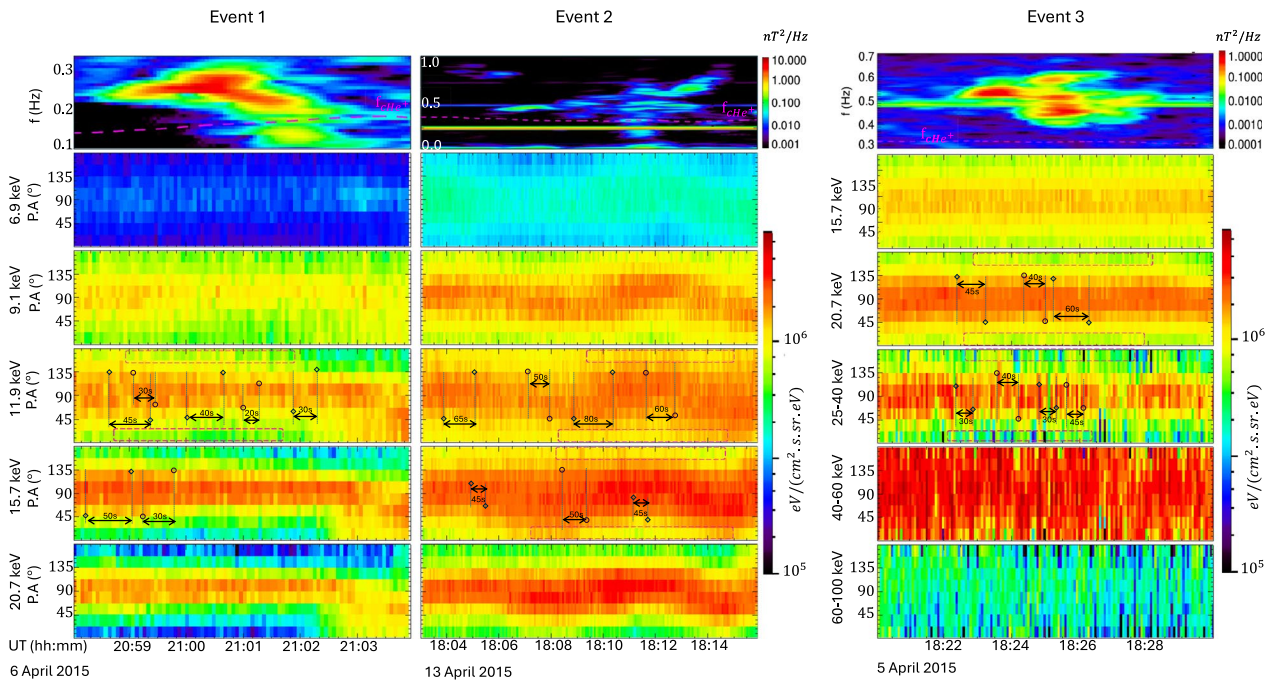
Ojha *et al. Earth, Planets and Space*      (2024) 76:81

Page 13 of 19



**Fig. 8** Proton pitch angle distribution (PAD) for three events. Pitch angles (PA) evolution in time for different proton energies where the color bar represents the flux of the protons. For reference, dynamic spectra of wave magnetic fields of each event are plotted on the top panel (where color bars are in $nT^2/Hz$). For Event 1 and Event 2, PAD shows 6.9 keV, 9.1 keV, 11.9 keV, 15.7 keV, and 20.7 keV protons; and for Event 3, 15.7 keV, 20.7 keV, 25–40 keV, 40–60 keV, and 60–100 keV protons are shown. Dashed line boxes in magenta highlight scattered proton populations in the lower pitch angles in both parallel and antiparallel directions. Two sets of vertical dashed lines with diamonds and circles indicate the half-bounce periods of protons. The half-bounce period for each set is written in seconds (s) in between the vertical lines

the particle scattering by the EMIC rising and falling tone is recognized prominently. For Event 1, we see proton flux enhancement around $90°$ before 21:00 UT. After that proton flux is reduced significantly (around 10–20% of the earliear population).

We denote magenta-colored rectangular boxes to indicate the scattered population, where the flux is higher (yellow or red pixels at lower pitch angles around 0–15° and 165–180°) in the antiparallel and parallel directions. These pixels indicate the scattering of the untrapped protons away from the 90°. It is worth noticing that the scattered proton fluxes in the lower pitch angles are more during the risng and falling tone period. We have shown the directional change of protons in Fig. 8 where we see both antiparallel and parallel proton flux. Closer inspection shows the protons are scattered into smaller pitch angles, hence with larger average velocities ($|V_R|$) in the parallel direction (from 21:00:30–21:01:30 UT, which is the falling tone timing). These protons at smaller pitch angles are essentially outside the nonlinear potential. There are a smaller number of protons inside than outside of the potential. This potential is known as a proton hole in velocity phase space and is responsible for the rising tone generation (Omura et al. 2010). Before

21:00 UT for event 1, a rising tone patch exists that can scatter the protons into smaller pitch angles, at parallel direction from $0°–15°$, and anti-parallaly $165°–180°$. These protons exhibit bounce motion, and we observed more fluxes around $135°$ and $45°$. The bounce mechanism is very important; however, to observe in PAD spectra is hard. For different $L$-values, energies, and pitch angles, bounce period will vary and thus we should see scattered fluxes along different pitch angles in the PADs. We identify the bouncing of the protons denoted by sets of two vertical dotted lines with two diamond shaped and circle shaped marks pointed at up and down to each line of a set. We choose two shapes (i.e., diamonds and circles) just to distinguish the sets better. The half-bounce period for each set is written in seconds (s) in between the vertical lines. There are bounce motions all over the PADs; however, we have shown some of their examples. Detailed comparison of these observed bounce periods with the theoretical calculated values is discussed later in the paper.

For Event 2, we show the PADs for the same energy channels as shown for Event 1. In this case, the scattered protons are also seen in the lower pitch angles denoted by magneta boxes in the energy channels 11.9 keV and
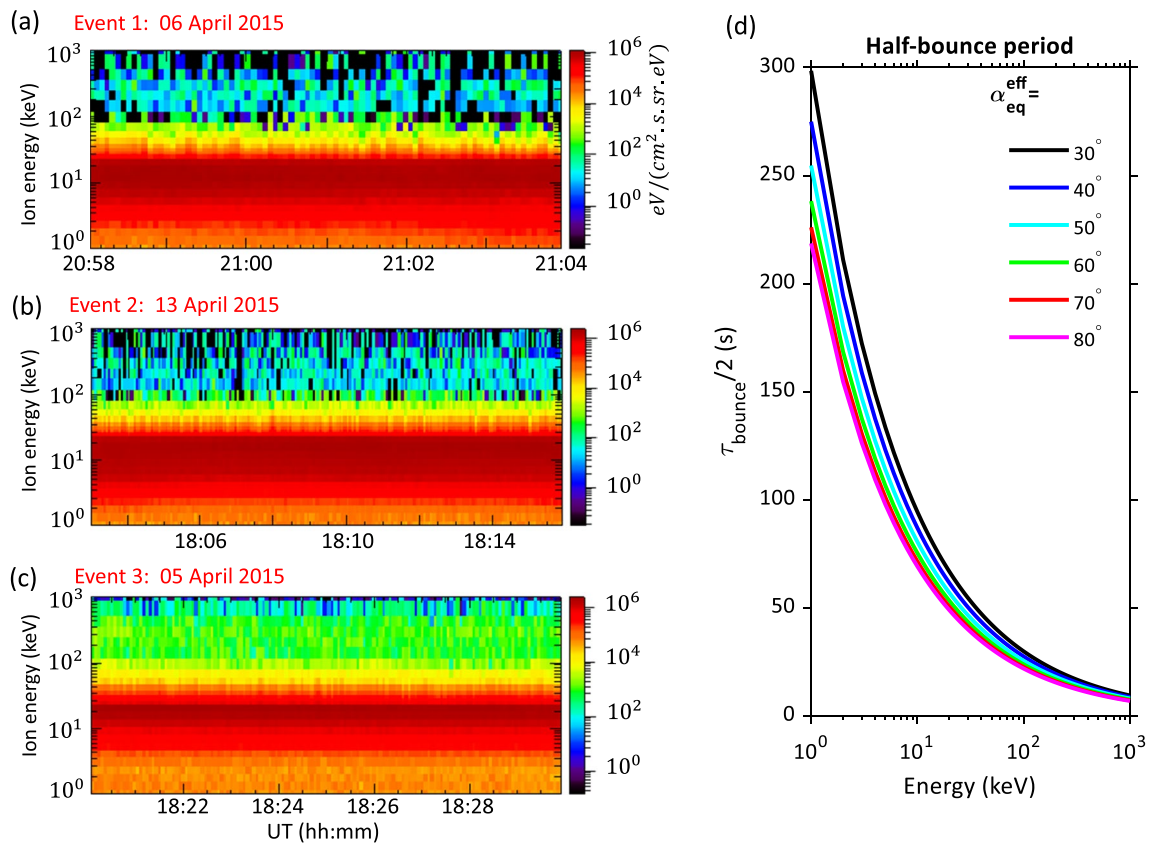
**Fig. 9** **a–c** ion energy flux showing for Events 1, 2, and 3, respectively. We see enhancement of ion fluxes in 5–25 keV for Events 1 and 2; 5–100 keV for Event 3. **d** Half-Bounce period ($\tau_{bounce}/2$) of energetic protons plotted as a function of energy 1–1000 keV for effective pitch angles ($\alpha_{eq}^{eff}$) from 30° to 80°

15.7 keV. A clear indication of the bounce motion of the protons is observed. To ensure the total number of protons are almost constant for the time period of the event, we have checked the SuperDARN radar data set for this event during the period of forming rising and falling tones and found no injection from the night side (Remya et al. (2020) and references therein). Otherwise, there should be uniform distribution around a 90° pitch angle. We can see the scattering of the protons by the EMIC waves as enhanced proton flux is observed after 18:10 UT (just before the falling tone occurred).

Finally, for Event 3, the most prominent feature is observed in the energy channels 20.7 keV and 25–40 keV. In this case also, the untrapped protons are scattered first and then bounced back at the same interaction region, where the existing EMIC subpackets further trap the scattered protons. Because of the trapping a density-enhanced structure called proton hill is formed in the velocity phase space (Shoji and Omura 2017; Shoji et al. 2021). The proton hill generates the EMIC falling tones. The trapped protons are guided to the wave resonance velocity. As the wave frequency starts decreasing, the

absolute value of the resonance velocity increases. Thus the falling tone further scatters the trapped protons into smaller pitch angles. The resolution of the ESA probe is 8 s and we believe our methodology of identification of the scattering process is efficient and also matches the duration of the rising and falling subpackets measured in the dynamic spectrum for each event. For Event 3, in 25–40 keV chanel, we observed more flux than the other two events in the parallel and antiparallel directions because the bounce period of these relatively high-energy protons is smaller than the other two events. These observed bounce periods for all the events match the theoretical bounce period calculation shown in Fig. 9d. Detailed comparison is discussed later in the paper. Thus, the observed PADs confirm the three phenomena, i.e., wave scattering, bounce motion, and wave trapping and scattering. Based on this understanding, we present a possible scenario for the simultaneous generation of rising and falling tones in the next section.

### Proton bounce motion model and generation of observed co-existing rising and falling tones

The ESA and SST instruments of THEMIS are used to analyze the particle data. As shown in Fig. 9a–c, the intense proton fluxes (at least two to three orders higher than the background count) are observed in all three events of the wave emissions. The minimum cyclotron resonance energy ($E_{Res}^{min}$) in Fig. 7 matches very well with the observed proton energy flux in Fig. 9a–c. For Events 1 and 2, we observe greater proton flux than the background in an energy range of ~5–25 keV, whereas, for Event 3, the greater flux is seen in 10–60 keV. We plot the bounce periods of the protons in Fig. 9 d for an energy range of 1–1000 keV for different pitch angles. We have calculated the effective pitch angle (the angles at which the effective nonlinear interaction happens) as follows.

$$\alpha_{eq}^{eff} = \arctan \frac{\sqrt{V_{tot}^2 - V_R^2}}{|V_R|} \qquad (1)$$

where $V_{tot} = \sqrt{2E/m_p}$, E is the energy of the protons and $m_p$ is the mass of protons. We have calculated the half-bounce period (from the equator to the northern hemisphere mirror point and back to the equator) of observed resonant protons for different energies. To be consistent for the other two events, we calculated $\tau_{bounce}$ (Baumjohann and Treumann 2012) (equation 3.14 of the book) by varying proton energies from 1–1000 keV for different pitch angles, $\alpha_{eq}^{eff} = 30° - 80°$ and plotted in Fig. 9d. The half-bounce period, $\tau_{bounce}/2$ varies from ~20–120 s for the observed proton energies. For example, in the case of Event 1, for $E = 5$–10 keV and $V_R = 400$ to 1000 km/s (from theoretical $V_R$ and from observed 2D proton velocity distribution (velocity along and across the magnetic field), we calculate $V_R$; not shown here) for the entire frequency range and we obtain $\alpha_{eq}^{eff} \simeq 30$ to 80° and the half-bounce period ($\tau_{bounce}/2$) ~80 s to 140 s, whereas, the event lasted for ~240 s. For example, satellite position for Event 1 is L=10, and for Event 2 and Event 3, L = 8; with this, for Event 1 the calculated $\tau_{bounce}/2$ of 12 keV protons with $\alpha_{eq}^{eff} = 30°$ is 85 s, and with $\alpha_{eq}^{eff} = 80°$ calculated $\tau_{bounce}/2 = 62$s. For Event 2, 12 keV protons with $\alpha_{eq}^{eff} = 30°$ and 80° calculated $\tau_{bounce}/2 = 67$s and 50 s, respectively; and for Event 3, for 20 keV protons with $\alpha_{eq}^{eff} = 30°$ and 80° calculated $\tau_{bounce}/2 = 52$s and 37 s, respectively. Because of $\alpha_{eq}^{eff}$ stays mostly $\simeq 45° - 80°$ except for very lower resonance velocity (~ 400–500 km/s), most of the time the $\tau_{bounce}/2 < 50$ s. Whereas the whole event last for ~240 s, we have closely looked at the HHT analysis plot (Fig. 3) for all events, and we measured timings where the wave amplitudes are high, and we find that the prominent subpacket duration is ~
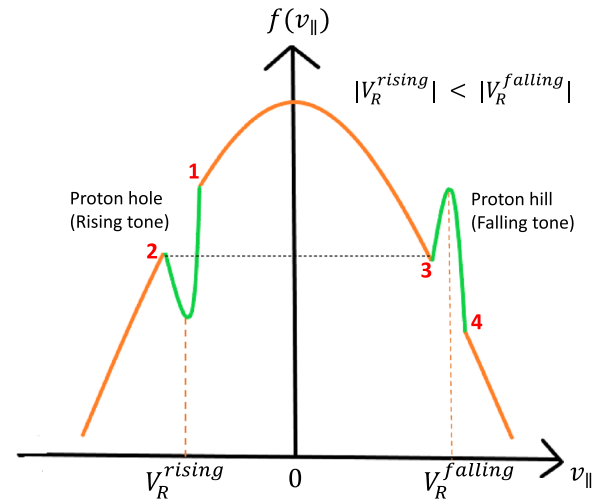


**Fig. 10** Schematic representation of proton velocity distribution function ($f(v_\parallel)$). The proton hole (proton hill) at the left (right) side of distribution generates the rising tone (falling tone)

20 s. Thus, during the propagation of the wave packets along the magnetic field, the protons can bounce back and forth, and the velocity distribution observed by the spacecraft particle detector can change. We see a good match between the observed values of the half bounce periods and the calculated values. The fact from Fig. 9d that the bounce period is a decreasing function of both effective pitch angle and the resonance energy, we must consider a range of bounce period values when we compare with the observation in PADs in 8. For all the events the observed bounce periods are 30–75 s, and the theoretical values are also fall in that range.

We have also examined the drifting of the protons in the azimuthal direction during the bounce motion. We have checked the drift period for $L = 10$ for 10 keV protons using Baumjohann and Treumann (2012), and for the range for half-bounce period mentioned here, i.e., for 20–120 s, the azimuthal drift varies from 0.006 $R_E$ – 0.039 $R_E$. This azimuthal drift is expected and well within the coherence limit ($< \sim 0.5$ $R_E$) as mentioned by Blum et al. (2017, 2016). Thus, the estimation of the bouncing effect of the protons are valid for these events we discussed.

A possible variation of the distribution function ($f(v_\parallel)$) which can generate co-existing rising and falling tones is schematically illustrated in Fig. 10. The plausible mechanism for their generation is as follows. At first, the protons enter point 1 (numbered 1 in red) and resonate with the triggering wave, forming the proton hole, which generates a rising tone EMIC subpacket. After the interaction with the triggering wave, protons are scattered towards smaller pitch angles with larger $v_\parallel$ at point

Ojha *et al. Earth, Planets and Space* (2024) 76:81

Page 16 of 19

2. From point 2, the scattered protons are bounced back and come to the other side of the distribution function at point 3. The bounced back protons are trapped by triggering waves traveling in the opposite direction and form a hill on the opposite side of the distribution function, resulting in the generation of falling tone emission. On the left-hand side of the distribution function, we expect a proton hole as $V_g$ is positive (forward). We expect a proton hill as $V_g$ is negative (backward) on the right-hand side. This scenario is observed for Events 1 and 2. On the other hand, for Event 3, the falling tone propagates parallel, and the rising tone propagates anti-parallelly (Fig. 5f). The rising tone interacts with the forward protons, whereas the falling tones with backward protons. We discuss it as a general scenario. It can be opposite where the proton hole can be on the right side, and the proton hill is on the left side of the distribution function. The magnitude of the resonance velocity of the falling tone is larger than that of the rising tone. The resonance velocity of the EMIC waves decreases with increasing frequency and tends to zero at the highest frequency of the emission. Thus, the observation presented in Fig. 8 is consistent with falling tones having a larger magnitude of the resonance velocity. The series of formations of proton holes and hills proceed in both forward and backward directions. As a consequence, we observe rising and falling tones together.

## Summary and discussion

We propose that the bounce motion of these protons, the period of which is of the order of the subpackets duration or less, can form a velocity distribution where the proton holes (related to rising tones) and hills (related to falling tones) are on opposite sides of the distribution. The evolution of this proton velocity distribution can generate these complex tones of EMIC waves simultaneously.

We summarize the process for the simultaneous observation of rising and falling tones below

(1) At first, the protons resonate with the triggering wave present, forming the proton hole generating a rising tone EMIC subpacket. These rising tone subpackets are thus initially present prior to the simultaneous rising and falling tone observations.

(2) The rising tones scatter the resonant protons into smaller pitch angles that lead to larger parallel velocities (i.e., larger $V_R$),

(3) These scattered protons with larger $V_R$ bounce back to the region where they interacted with the wave packets.

(4) Thus, proton hills are formed in velocity phase-space, and generation of falling tones occurs with $|V_R^{rising}| < |V_R^{falling}|$.

We investigated complex structures of EMIC waves where we found simultaneous rising and falling tones. For all the events, the energetic ions are either drifting from the night side due to substorm injection or due to dayside magnetopause reconnection. In Event 1, continuity between the rising and falling tones is observed. The wave properties are consistent with the typical EMIC waves. In Event 2, the structure between 18:08–18:11 UT still needs to be fully understood. There is a discontinuity of wave power between the rising tones that started earlier at 18:06 UT and later at 18:12 UT. We interpret the patch at 18:06 UT as the triggering wave due to the linear growth. Lastly, the whole structure is even more complex in Event 3. The patch during 18:23–18:24 UT can serve as the triggering wave for the simultaneous rising and falling tones observed later. We discuss Event 1 in detail, whereas the other events have the same characteristics. We assume a bi-Maxwellian distribution function of the energetic protons with $T_\perp > T_\parallel$ as defined in the dispersion solver named Kyoto University Plasma Dispersion Analysis Package [KUPDAP; Sugiyama et al. (2015)]. Assuming a bi-Maxwellian distribution function with $V_\perp = 776.67$ km.s$^{-1}$ and $V_\parallel = 579.18$ km .s$^{-1}$, for parallel propagation, i.e., $\theta=0°$, we find the linear growth rate becomes positive over a range of frequencies showing a maximum at $\omega/\Omega_p = 0.4$ (where $\Omega_p = 2\pi*0.7$ rad/s). The positive growth rate in the proton band suggests the triggering process at the beginning of the events. Linear growth is required at the low frequencies where the wave starts to grow. Thereafter once the amplitude of the linear growth reaches the threshold amplitude of the nonlinear growth, the wave starts to grow rapidly (Ojha et al. 2021). The presence of a triggering wave at the beginning of the event is consistent in all the events.

We have provided the possible mechanism for the fine structures, i.e., simultaneous rising and falling tone EMIC waves through the case study of three events. Regardless of the small frequency width we have shown here, i.e., 0.2–0.27 Hz (for the 1st event), 0.1–1 Hz (for the 2nd event), and 0.4–0.7 Hz (for the 3rd event), the nonlinear growth is substantial. According to the nonlinear wave growth theory by Omura et al. (2010), resonant interaction between the wave and the particles should satisfy the second-order nonlinear differential equation (equation (39) of Omura et al. (2010)) and the wave growth occurs nonlinearly when $|S| < 1$, where $S$ is the inhomogeneity factor, which is positive or negative for wave growth of rising and falling tone, respectively. We have calculated the variation of S with respect to frequency spread for each event and found the values of $|S|$ at the central frequencies of the first, second, and third events which are 0.015, 0.5, and 0.1, respectively (not shown

here). Thus, the importance of nonlinear wave growth is substantiated.

Recently, Liu et al. (2021) reported an observation of rising chorus emissions with falling sub-elements. They have presented two events that study both the upper and lower band chorus emissions with the clear existence of falling tones. Chen et al. (2023) reproduced the observation of Liu et al. (2021) by the 1-D general curvilinear PIC (gcPIC) simulation and they show that during an interval of rising and falling frequency chirping, both the electron hill and hole can form around the resonance velocities. Very recently, Nogi and Omura (2023) reported in their simulation, the generation of a rising tone chorus accompanied by traces of falling tones (Fig. 11 of their paper). In all these observations and simulations, the rising and falling tones have the same direction of the group velocity. Thus, the simultaneous generation of rising and falling chorus elements can be found. Unlike the observation of chorus rising and falling sub-elements, in this paper, we address the general trend of the EMIC wave emissions. In our observations, in all three cases, the rising and falling tones propagate in opposite directions, which is further supported by the bounce-back mechanism of the resonant protons and the formation of proton holes and hills on the opposite side of the velocity distribution function. However, one may closely look into the Poynting flux spectrum for all the events and find traces of frequencies rising and falling with the same Poynting flux direction. We are unable to identify them clearly due to the limitation of the low resolution data. High-resolution data is required to identify the same directional propagation of rising and falling subpackets.

While the rising tone emissions and their impacts on the magnetosphere have been well explored, the effect of falling tones is not investigated much. Further, the combined effect of the rising and falling tones on the energetic particle precipitation should be studied in the future. A statistical study is required for understanding the complex nature of the occurrence of the simultaneous rising and falling tone EMIC waves.

## Abbreviations
EMIC    Electromagnetic Ion Cyclotron
PADs    Pitch angle distributions

## Declarations

### Competing interests
The authors declare that they have no competing interests.

### Author details
[1]Northumbria University, Newcastle Upon Tyne, United Kingdom NE1 8ST. [2]Research Institute for Sustainable Humanosphere, Kyoto University, Uji, Kyoto 611-0011, Japan. [3]Indian Institute of Geomagnetism (IIG), Navi Mumbai, India. [4]Retired, Vashi, Navi Mumbai 400703, India.

## References
Allen RC, Zhang J-C, Kistler LM, Spence HE, Lin R-L, Klecker B, Jordanova VK (2015) A statistical study of emic waves observed by cluster: 1. wave properties. J Geophys Res: Space Phys 120(7):5574–5592. https://doi.org/10.1002/2015JA021333

Angelopoulos V, Cruce P, Drozdov A, Grimes EW, Hatzigeorgiu N, King DA, Schroeder P (2019) The space physics environment data analysis system (SPEDAS). Space Sci Rev. https://doi.org/10.1007/s11214-018-0576-4

Auster HU, Glassmeier KH, Magnes W, Aydogar O, Baumjohann W, Constantinescu D, Wiedemann M (2008) The themis fluxgate magnetometer. Space Sci Rev 141(1):235–264. https://doi.org/10.1007/s11214-008-9365-9

Baumjohann W, Treumann RA (2012) Basic space plasma physics 671. IMPERIAL COLLEGE PRESS, London

Blum LW, Agapitov O, Bonnell JW, Kletzing C, Wygant J (2016) EMIC wave spatial and coherence scales as determined from multipoint van allen probe measurements. Geophys Res Lett 43(10):4799–4807. https://doi.org/10.1002/2016gl068799

Blum LW, Bonnell JW, Agapitov O, Paulson K, Kletzing C (2017) EMIC wave scale size in the inner magnetosphere: observations from the dual van allen probes. Geophys Res Lett 44(3):1227–1233. https://doi.org/10.1002/2016gl072316

Bonnell J, Mozer F, Delory G, Hull A, Ergun R, Cully C, . . . Harvey P (2009) The electric field instrument (efi) for themis. The THEMIS mission, 303–341

Chen H, Wang X, Chen L, Omura Y, Lu Q, Chen R, Gao X (2023) Simulation of downward frequency chirping in the rising tone chorus element. Geophys Res Lett. https://doi.org/10.1029/2023gl103160

Chen L, Thorne RM, Bortnik J, Zhang X-J (2016) Nonresonant interactions of electromagnetic ion cyclotron waves with relativistic electrons. J Geophys Res: Space Phys 121(10):9913–9925. https://doi.org/10.1002/2016ja022813

Clilverd MA, Duthie R, Hardman R, Hendry AT, Rodger CJ, Raita T, Milling DK (2015) Electron precipitation from EMIC waves: a case study from 31 May 2013. J Geophys Res: Space Phys 120(5):3618–3631. https://doi.org/10.1002/2015JA021090

Engebretson M, Lessard M, Bortnik J, Green J, Horne RB, Detrick D et al (2008) Pc1-pc2 waves and energetic particle precipitation during and after

Ojha *et al. Earth, Planets and Space*        (2024) 76:81

Page 18 of 19

magnetic storms: superposed epoch analysis and case studies. J Geophys Res: Space Phys. https://doi.org/10.1029/2007JA012362

Gendrin R, Ashour-Abdalla M, Omura Y, Quest K (1984) Linear analysis of ion cyclotron interaction in a multicomponent plasma. J Geophys Res 89(A10):9119. https://doi.org/10.1029/ja089ia10p09119

Grison B, Hanzelka M, Breuillard H, Darrouzet F, Santol'ık O, CornilleauWehrlin N, Dandouras I (2018) Plasmaspheric plumes and EMIC rising tone emissions. J Geophys Res: Space Phys 123(11):9443–9452. https://doi.org/10.1029/2018ja025796

Grison B, Santolik O, Cornilleau-Wehrlin N, Masson A, Engebretson M, Pickett J, Nomura R (2013) EMIC triggered chorus emissions in cluster data. J Geophys Res: Space Phys 118(3):1159–1169. https://doi.org/10.1002/jgra.50178

Hendry AT, Santolik O, Kletzing CA, Rodger CJ, Shiokawa K, Baishev D (2019) Multi-instrument observation of nonlinear EMIC-driven electron precipitation at sub-MeV energies. Geophys Res Lett 46(13):7248–7257. https://doi.org/10.1029/2019gl082401

Horne RB, Thorne RM (1993) On the preferred source location for the convective amplification of ion cyclotron waves. J Geophys Res: Space Phys 98(A6):9233–9247

Huang NE (2014) Hilbert-huang transform and its applications. World Scientific, Singapore

Huang NE, Shen Z, Long SR, Wu MC, Shih HH, Zheng Q, Liu HH (1998) The empirical mode decomposition and the hilbert spectrum for nonlinear and non-stationary time series analysis. Proceedings of the Royal Society of London. Series A: mathematical, physical and engineering sciences, 454 (1971), 903–995

Jackson LB (1989) Digital filters and signal processing. Springer, Berlin

Kakad B, Omura Y, Kakad A, Upadhyay A, Sinha AK (2018) Characteristics of subpacket structures in ground EMIC wave observations. J Geophys Res: Space Phys 123(10):8358–8376. https://doi.org/10.1029/2018JA025473

Katoh Y, Kitahara M, Kojima H, Omura Y, Kasahara S, Hirahara M, Miyoshi Y, Seki K, Asamura K, Takashima T, Ono T (2013) Significance of wave-particle interaction analyzer for direct measurements of nonlinear wave-particle interactions. Ann Geophys. https://doi.org/10.5194/angeo-31-503-2013

Kivelson MG, Russell CT (1995) Introduction to space physics. Cambridge University Press, Cambridge

Kozyra JU, Cravens TE, Nagy AF, Fontheim EG, Ong RSB (1984) Effects of energetic heavy ions on electromagnetic ion cyclotron wave generation in the plasmapause region. J Geophys Res 89(A4):2217. https://doi.org/10.1029/ja089ia04p02217

Kubota Y, Omura Y, Summers D (2015) Relativistic electron precipitation induced by EMIC-triggered emissions in a dipole magnetosphere. J Geophys Res: Space Phys 120(6):4384–4399. https://doi.org/10.1002/2015JA021017

Liu S, Gao Z, Xiao F, He Q, Li T, Shang X, Zhang S (2021) Observation of unusual chorus elements by van allen probes. J Geophys Res: Space Phys. https://doi.org/10.1029/2021ja029258

McCollough J, Elkington S, Usanova M, Mann I, Baker D, Kale Z (2010) Physical mechanisms of compressional emic wave growth. J Geophys Res: Space Phys. https://doi.org/10.1029/2010JA015393

McFadden JP, Carlson CW, Larson D, Ludlam M, Abiad R, Elliott B, Angelopoulos V (2008) The THEMIS ESA plasma instrument and in-flight calibration. Space Sci Rev 141(1–4):277–302. https://doi.org/10.1007/s11214-008-9440-2

Mitra SK (2006) Digital signal processing : a computer based approach. McGraw-Hill, New York

Nakamura S, Omura Y, Angelopoulos V (2016) A statistical study of EMIC rising and falling tone emissions observed by themis. J Geophys Res: Space Phys 121(9):8374–8391. https://doi.org/10.1002/2016JA022353

Nakamura S, Omura Y, Kletzing C, Baker DN (2019) Rapid precipitation of relativistic electron by EMIC rising-tone emissions observed by the van allen probes. J Geophys Res: Space Phys 124(8):6701–6714. https://doi.org/10.1029/2019ja026772

Nakamura S, Omura Y, Machida S, Shoji M, Nos'e M, Angelopoulos V (2014) Electromagnetic ion cyclotron rising tone emissions observed by themis probes outside the plasmapause. J Geophys Res: Space Phys 119(3):1874–1886. https://doi.org/10.1002/2013JA019146

Nakamura S, Omura Y, Shoji M, Nos'e M, Summers D, Angelopoulos V (2015) Subpacket structures in EMIC rising tone emissions observed by the themis probes. J Geophys Res: Space Phys 120(9):7318–7330. https://doi.org/10.1002/2014JA020764

Ni B, Cao X, Zou Z, Zhou C, Gu X, Bortnik J, Xie L (2015) Resonant scattering of outer zone relativistic electrons by multiband EMIC waves and resultant electron loss time scales. J Geophys Res: Space Phys 120(9):7357–7373. https://doi.org/10.1002/2015ja021466

Nogi T, Omura Y (2021) Nonlinear signatures of VLF-triggered emissions: a simulation study. J Geophys Res: Space Phys. https://doi.org/10.1029/2021ja029826

Nogi T, Omura Y (2023) Upstream shift of generation region of whistler mode rising-tone emissions in the magnetosphere. J Geophys Res: Space Phys. https://doi.org/10.1029/2022ja031024

Nomura R, Shiokawa K, Omura Y, Ebihara Y, Miyoshi Y, Sakaguchi K, Connors M (2016) Pulsating proton aurora caused by rising tone pc1 waves. J Geophys Res: Space Phys 121(2):1608–1618. https://doi.org/10.1002/2015ja021681

Ojha B, Omura Y, Singh S, Lakhina GS (2021) Multipoint analysis of source regions of EMIC waves and rapid growth of subpackets. J Geophys Res: Space Phys. https://doi.org/10.1029/2021ja029514

Omura Y (2021) Nonlinear wave growth theory of whistler-mode chorus and hiss emissions in the magnetosphere. Earth, Planets Space. https://doi.org/10.1186/s40623-021-01380-w

Omura Y, Pickett J, Grison B, Santolik O, Dandouras I, Engebretson M, Masson A (2010) Theory and observation of electromagnetic ion cyclotron triggered emissions in the magnetosphere. J Geophys Res: Space Phys. https://doi.org/10.1029/2010JA015300

Omura Y, Zhao Q (2012) Nonlinear pitch angle scattering of relativistic electrons by EMIC waves in the inner magnetosphere. J Geophys Res: Space Phys. https://doi.org/10.1029/2012JA017943

Omura Y, Zhao Q (2013) Relativistic electron microbursts due to nonlinear pitch angle scattering by EMIC triggered emissions. J Geophys Res: Space Phys 118(8):5008–5020. https://doi.org/10.1002/jgra.50477

Pickett JS, Grison B, Omura Y, Engebretson MJ, Dandouras I, Masson A, Constantinescu D (2010) Cluster observations of EMIC triggered emissions in association with pc1 waves near earth's plasmapause. Geophys Res Lett. https://doi.org/10.1029/2010gl042648

Remya B, Tsurutani B, Reddy R, Lakhina G, Hajra R (2015) Electromagnetic cyclotron waves in the dayside subsolar outer magnetosphere generated by enhanced solar wind pressure: EMIC wave coherency. J Geophys Res: Space Phys 120(9):7536–7551. https://doi.org/10.1002/2015JA021327

Remya B, Sibeck DG, Ruohoniemi JM, Kunduri B, Halford AJ, Reeves GD, Reddy V (2020) Association between EMIC wave occurrence and enhanced convection periods during ion injections. Geophys Res Lett. https://doi.org/10.1029/2019GL085676

Saikin AA, Zhang J, Allen RC, Smith CW, Kistler LM, Spence HE, Jordanova VK (2015) The occurrence and wave properties of H+, He+, and O+-band EMIC waves observed by the van allen probes. J Geophys Res: Space Phys 120(9):7477–7492. https://doi.org/10.1002/2015JA021358

Sakaguchi K, Shiokawa K, Miyoshi Y, Connors M (2015) Isolated proton auroras and pc1/emic waves at subauroral latitudes. Auror Dyn Space Weather 215:59

Shabansky V (1971) Some processes in the magnetosphere. Space Sci Rev 12(3):299–418

Shoji M, Miyoshi Y, Katoh Y, Keika K, Angelopoulos V, Kasahara S, Omura Y (2017) Ion hole formation and nonlinear generation of electromagnetic ion cyclotron waves: themis observations. Geophys Res Lett 44(17):8730–8738

Shoji M, Miyoshi Y, Kistler LM, Asamura K, Matsuoka A, Kasaba Y, Shinohara I (2021) Discovery of proton hill in the phase space during interactions between ions and electromagnetic ion cyclotron waves. Sci Rep. https://doi.org/10.1038/s41598-021-92541-0

Shoji M, Miyoshi Y, Omura Y, Kistler LM, Kasaba Y, Matsuda S et al (2018) Instantaneous frequency analysis on nonlinear emic emissions: arase observation. Geophys Res Lett 45(24):13–199

Shoji M, Omura Y (2011) Simulation of electromagnetic ion cyclotron triggered emissions in the earth's inner magnetosphere. J Geophys Res: Space Phys. https://doi.org/10.1029/2010ja016351

Shoji M, Omura Y (2013) Triggering process of electromagnetic ion cyclotron rising tone emissions in the inner magnetosphere. J Geophys Res: Space Phys 118(9):5553–5561

Shoji M, Omura Y (2017) Nonlinear generation mechanism of EMIC falling tone emissions. J Geophys Res: Space Phys 122(10):9924–9933. https://doi.org/10.1002/2017ja023883

Shprits YY, Chen L, Thorne RM (2009) Simulations of pitch 834 angle scattering of relativistic electrons with MLT-dependent diffusion coefficients. J Geophys Res: Space Phys. https://doi.org/10.1029/2008ja013695

Shue J-H, Song P, Russell CT, Steinberg JT, Chao JK, Zastenker G, Kawano H (1998) Magnetopause location under extreme solar wind conditions. J Geophys Res: Space Phys 103(A8):17691–17700. https://doi.org/10.1029/98ja01103

Sibeck DG, McEntire RW, Lui ATY, Lopez RE, Krimigis SM (1987) Magnetic field drift shell splitting: cause of unusual dayside particle pitch angle distributions during storms and substorms. J Geophys Res 92(A12):13485. https://doi.org/10.1029/ja092ia12p13485

Stix TH (1962) Waves in Plasmas

Sugiyama H, Singh S, Omura Y, Shoji M, Nunn D, Summers D (2015) Electromagnetic ion cyclotron waves in the earth's magnetosphere with a kappa-maxwellian particle distribution. J Geophys Res: Space Phys 120(10):8426–8439. https://doi.org/10.1002/2015JA021346

Summers D, Thorne RM (2003) Relativistic electron pitch-angle scattering by electromagnetic ion cyclotron waves during geomagnetic storms. J Geophys Res: Space Phys. https://doi.org/10.1029/2002JA009489

Summers D, Thorne RM, Xiao F (1998) Relativistic theory of wave-particle resonant diffusion with application to electron acceleration in the magnetosphere. J Geophys Res: Space Phys 103(A9):20487–20500. https://doi.org/10.1029/98JA01740

Thorne RM, Kennel C (1971) Relativistic electron precipitation during magnetic storm main phase. J Geophys Res 76(19):4446–4453. https://doi.org/10.1029/JA076i019p04446

Tsyganenko NA (2005) Modeling the dynamics of the inner magnetosphere during strong geomagnetic storms. J Geophys Res. https://doi.org/10.1029/2004ja010798

Usanova ME, Drozdov A, Orlova K, Mann IR, Shprits Y, Robertson MT, Wygant J (2014) Effect of EMIC waves on relativistic and ultrarelativistic electron populations: ground-based and van allen probes observations. Geophys Res Lett 41(5):1375–1381. https://doi.org/10.1002/2013gl059024

Vines S, Allen R, Anderson B, Engebretson M, Fuselier S, Russell C et al (2019) Emic waves in the outer magnetosphere: observations of an off-equator source region. Geophys Res Lett 46(11):5707–5716

Zhang X-J, Li W, Ma Q, Thorne RM, Angelopoulos V, Bortnik J, Fennell JF (2016) Direct evidence for EMIC wave scattering of relativistic electrons in space. J Geophys Res: Space Phys 121(7):6620–6631. https://doi.org/10.1002/2016ja022521

Zhu H, Chen L, Claudepierre SG, Zheng L (2020) Direct evidence of the pitch angle scattering of relativistic electrons induced by emic waves. Geophys Res Lett. https://doi.org/10.1029/2019GL085637

Zhang Hui, Zong Qiugang, Connor Hyunju, Peter A, Gabor Delamere, Han Facsko Desheng, Hasegawa Hiroshi, Kallio Esa, Kis Árpád, Le Guan, Bertrand Lembège Yu, Lin Terry Z, Liu Kjellmar Oksavik, Omidi Nojan, Otto Antonius, Ren Jie, Shi Quanqi, David G, Yao Sibeck Shutao (2022) Dayside transient phenomena and their impact on the magnetosphere and ionosphere. Space Sci Rev. https://doi.org/10.1007/s11214-021-00865-0

## Publisher's Note